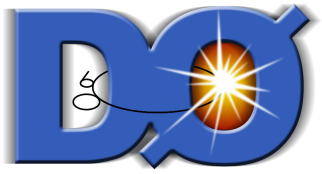

D0 Note 6240-CONF

Measurement of the Cross Section for $p\bar{p} \to Z\gamma \to \mu\mu\gamma$ at $\sqrt{s} = 1.96$ TeV

The D0 Collaboration
URL http://www.fnal.gov
(Dated: September 13, 2011)

We present a measurement of the $p\bar{p} \to Z\gamma \to \mu\mu\gamma$ cross section at $\sqrt{s} = 1.96$ TeV using a data sample corresponding to an integrated luminosity of 6.2 fb^{-1} collected by the D0 experiment at the Fermilab Tevatron Collider. For photon transverse momentum $p_T^\gamma > 10$ GeV/c, we observe 1000 $Z\gamma$ candidates, and 308 $Z\gamma$ candidates with the three-body invariant mass $M_{\mu\mu\gamma} > 110$ GeV/c^2. The data are corrected for signal acceptance and resolution after background subtraction to yield a resolution-unfolded differential cross section $d\sigma/dp_T^\gamma$. Both the total production cross section and the unfolded differential distribution are consistent with the MCFM next-to-leading-order prediction of the standard model.

Preliminary Results for Summer 2011 Conferences

I. INTRODUCTION

The standard model (SM) describes the electroweak interaction through a non-abelian gauge group $SU(2)_L \otimes U(1)_Y$, which provides self-interactions of gauge bosons. The Z boson, however, carries no weak hypercharge nor weak isospin, and $Z\gamma$ couplings are therefore not permitted. The production of $Z\gamma$ systems in the SM is dominated by the lowest-order Feynman diagrams shown in Fig. I.

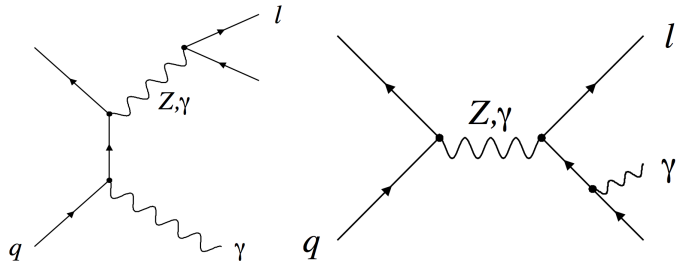

(a) ISR (b) FSR

FIG. 1: The lowest-order SM process of $Z(\gamma) \to ll + \gamma$ production: (a) initial-state radiation, and (b) final-state radiation.

To check for anomalous contributions to $Z\gamma$ production, we measure the total production and differential cross section $d\sigma/dp_T^\gamma$ and compare the results with SM predictions.

II. DATA SELECTION

The D0 detector [1] consists of a central tracker, electromagnetic and hadronic calorimeters, and muon detectors. The central tracker is designed to measure trajectories of charged particles and contains a central region of silicon microstrip (SMT) detectors and an outer region of scintillating fiber (CFT) detectors. The SMT detectors consist of five to six layers of double sided silicon wafers arranged cylindrically about the beam pipe and interleaved with multiple annular disks oriented perpendicular to the beam (z) axis. The CFT detectors consist of ribbons of sixteen double layers of scintillating fibers mounted outside the SMT detector. The tracking detector is embedded in a 1.9 T solenoidal magnet, which is surrounded by a liquid-argon-Uranium calorimeter that contains a fine grained electromagnetic section. Similar calorimeters in the forward regoin cover angles down to 2 to 3 degrees relative to the beam axis. Central preshower (CPS) detectors, constructed of several layers of triangular scintillator strips, are positioned in front of the electromagnetic calorimeter. The calorimeters are surrounded by a muon detection system consisting of three layers of tracking detectors, scintillation trigger counters, and 1.8 T toroid magnets.

The data sample used corresponds to an integrated luminosity of 6.2 fb^{-1} collected by the D0 experiment in Run IIb of the Fermilab Tevatron. The $Z\gamma$ events are selected in the $\mu^+\mu^-\gamma$ ($\mu\mu\gamma$ henceforth) final-state, where the muons are detected in both the central tracker and the outer muon detectors within $|\eta| < 2$, and the photon is reconstructed in the central electromagnetic calorimeter within $|\eta| < 1.1$, where η is the pseudorapidity defined with respect to the geometrical center of the detector and the beam line (the z axis). We select Z candidate events that satisfy at least one of a suite of high-p_T inclusive single-muon triggers. Two oppositely charged muon candidates are required per event, both of which must have reconstructed transverse momentum $p_T > 15$ GeV/c and be matched to a track in the central tracker with at least one hit in the SMT detectors. At least one of the muons must have $p_T > 20$ GeV/c, and the tracks must be well isolated within the calorimeters and in the central trackers. Both muon candidates are required to originate from within 2 cm of the interaction point in the z direction. Finally, we require the invariant mass of the two muons to be $M_{\mu\mu} > 60$ GeV/c^2. For simplicity, we refer to Z/γ^* dimuon pairs with $M_{\mu\mu} > 60$ GeV/c^2 as Z bosons.

Candidate $\mu\mu\gamma$ events are defined by a muon pair that passes the above selections and a photon candidate as a well-isolated cluster within the central electromagnetic calorimeter and at least 90% of the total energy deposition in the electromagnetic section of the calorimeter. Candidate electromagnetic calorimeter clusters are required to be reconstructed within a cone of radius $\Delta\mathcal{R} = \sqrt{(\Delta\phi)^2 + (\Delta\eta)^2} < 0.2$ about its axis, where ϕ is the azimuth. The photon energy is defined as the total energy within a cone $\Delta\mathcal{R} < 0.2$, and we impose an isolation criterion on other energy deposition by requiring that the energy within the annular region $0.2 < \Delta\mathcal{R} < 0.4$ is less than 15% of the total cluster energy and that the scalar sum of charged-track transverse momentum within $0.05 < \Delta\mathcal{R} < 0.4$ about

the cluster is less than 2 GeV/c. The measured transverse momentum of the photon candidate p_T^γ must exceed 10 GeV/c and be separated from the closest candidate muon by $\Delta\mathcal{R} > 0.7$.

Because quarks and gluons can hadronize to jets containing high-p_T electromagnetic objects and thereby mimic a photon signal, we require the photon candidate to pass a minimal output of an artificial neural network output that favors a photon hypothesis over a jet hypothesis. The artificial neural network utilizes five variables from the tracking detector, the calorimeter, and the CPS detectors that provide for a robust differentiation between photons and jets [2].

In total, we select 253,175 $\mu\mu$ events that contain a sub-sample of 1000 $\mu\mu\gamma$ events. To minimize the contribution from FSR in the $Z\gamma$ signal, we define a second subsample with 308 selected events that requires a three-body invariant mass $M_{\mu\mu\gamma} > 110$ GeV/c^2.

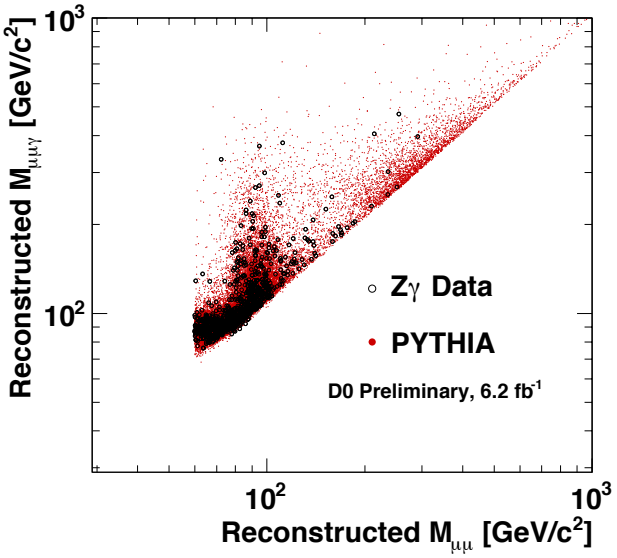

FIG. 2: The reconstructed two-body invariant mass, $M_{\mu\mu}$, versus the reconstructed three-body invariant mass, $M_{\mu\mu\gamma}$, for all 1000 $\mu\mu\gamma$ candidate events. The data (black) are overlaid on a PYTHIA simulation containing FSR and ISR (red).

III. MONTE CARLO SIMULATION

We use approximately 40M inclusive $Z/\gamma^* \to \mu\mu$ simulated events to estimate the acceptance and efficiency of the detector. The events are generated by PYTHIA v6.409 with photon radiation turned on [3] and the CTEQ6.1L parton distribution functions (PDF). Because PYTHIA is a leading-order (LO) generator and does not reproduce the observed p_T^Z spectrum in data, generated events are reweighted to reflect the p_T^Z distribution observed in Ref. [4]. Events are then traced through the D0 detector using a simulation based on GEANT3 [5]. Data events from random beam crossings are overlaid on the simulated interactions to reproduce the effects of multiple $p\bar{p}$ interactions and detector noise. Simulated interactions are assigned weights that take account of observed differences between data and simulation, e.g., z coordinate of the vertex, instantaneous luminosity, trigger efficiency, muon identification (ID) efficiency, photon ID efficiency, and resolution effects. The reconstruction and selection of simulated events are identical to those described above for data.

Figure 2 shows the dimuon invariant mass $M_{\mu\mu}$ vs. $M_{\mu\mu\gamma}$ for the 1000 $\mu\mu\gamma$ events. Events with $M_{\mu\mu} < M_Z$ and $M_{\mu\mu\gamma} \approx M_Z$ result most likely from FSR. In what follows, we present the data with and without a requirement of $M_{\mu\mu\gamma} > 110$ GeV/c^2 to demonstrate the contribution of FSR in the data.

IV. BACKGROUND SUBTRACTION

The dominant background for $Z\gamma$ production is from Z+jet events, with the jet mimicking a photon. We utilize a data-driven method to subtract this background, i.e., estimate the number of signal events in the data sample.

The "matrix method" estimates the contribution of signal events in the data sample by changing the output cutoff on the artificial neural network output (O_{NN}) from the initial value to a more restrictive value: $n_i \to n_r$. As shown in Eq. (1), the number of events passing the more restrictive requirement, in terms of the number that pass the looser requirements (N_γ and N_{jet}), can be written as follows:

$$\begin{aligned} N_{data}\ (O_{NN} > n_i) &= N_\gamma + N_{jet}, \\ N_{data}\ (O_{NN} > n_r) &= \epsilon_\gamma N_\gamma + \epsilon_{jet} N_{jet}, \end{aligned} \tag{1}$$

where the efficiencies for photons and jets to pass the tighter requirement, ϵ_γ and ϵ_{jet}, are determined through pure photon and jet PYTHIA simulations, respectively. Solving these linear equations, we obtain N_γ and N_{jet}, the number of signal and background events in the less restrictive data sample, $N_{data}\ (O_{NN} > n_i)$. We estimate 1.5% and 10% systematic uncertainties on ϵ_γ and ϵ_{jet} by comparing the photon and jet simulation with photon and jet data. With no $M_{\mu\mu\gamma}$ requirement, the matrix method predicts 946.8 ± 40.1 (stat.) ± 16.0 (syst.) $Z\gamma$ events. For $M_{\mu\mu\gamma} > 110$ GeV/c^2, we obtain 266.7 ± 23.6 (stat.) ± 1.7 (syst.) $Z\gamma$ events.

We use a second procedure (the "template method") to estimate the number of $Z\gamma$ signal events in the data by using PYTHIA to generate pure photon and pure jet templates and study these as a function of O_{NN} by fitting contributions of photon and jet templates to the data, using a binned one-dimensional log-likelihood to extract the relative fractions of photons events in the sample. Contributions to the statistical uncertainty on the final result include the uncertainty on the fitted parameter and the Poisson uncertainty on the total number of events in the data. These uncertainties are added in quadrature to provide an estimation of the total statistical uncertainty. The systematic uncertainties of 1.5% and 10% on the extracted N_γ are based on the shape of the O_{NN} distribution of photons and jets, respectively, and are estimated by comparing the simulation to photon and jet data. The number of $Z\gamma$ events is found to be 925.7 ± 39.5 (stat.) ± 15.7 (syst.). For $M_{\mu\mu\gamma} > 110$ GeV/c^2, we estimate the number of $Z\gamma$ events to be 258.3 ± 22.7 (stat.) ± 6.8 (syst.). Results for the fits with and without the $M_{\mu\mu\gamma} > 110$ GeV/c^2 requirement are shown in Fig. 3 and Fig. 4. The measured values are consistent with those from the matrix method. We also perform fits to the data for each bin of p_T^γ and again find the results of the two methods consistent. The output from the template method is used to calculate the total cross section and the matrix method to obtain the differential cross section $d\sigma/dp_T^\gamma$.

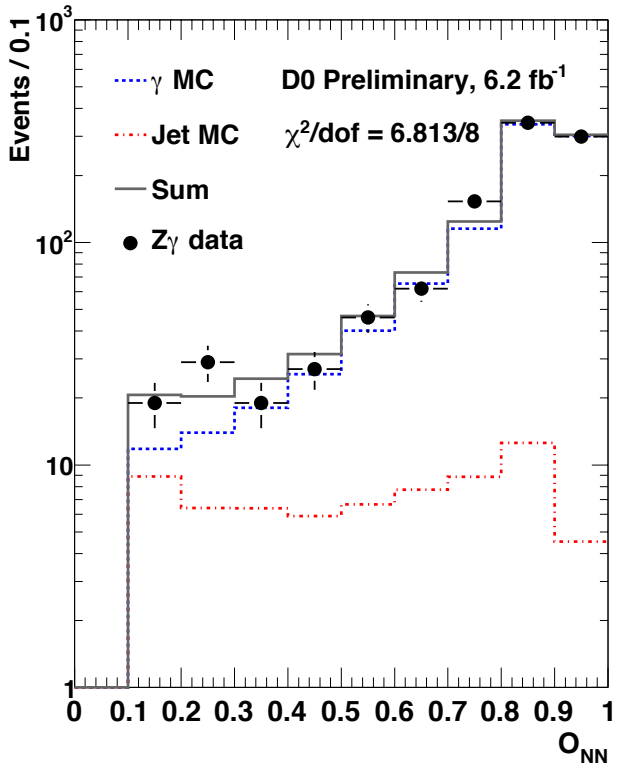

FIG. 3: Fits to all data with a mixture of photon and jet templates as a function of the output of the neural network, O_{NN}.

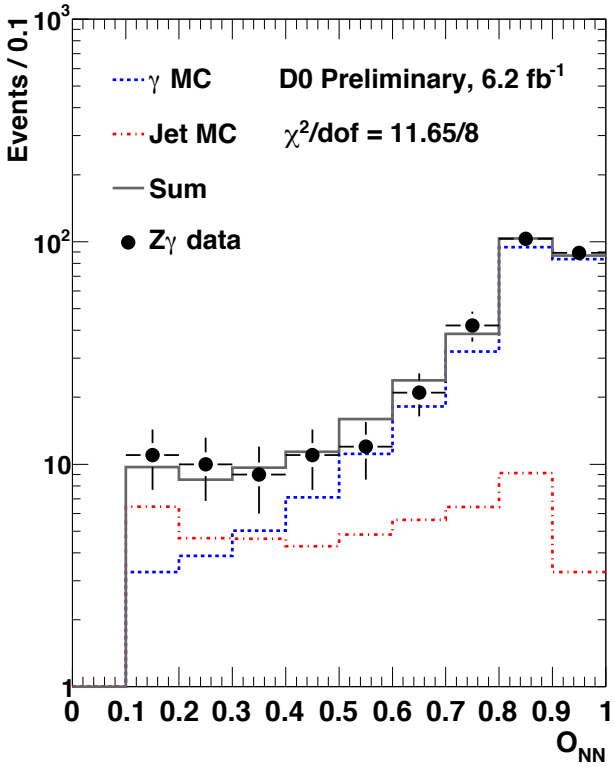

FIG. 4: Fits to all data with a mixture of of photon and jet templates as a function of the output of the neural network, O_{NN}, for the requirement $M_{\mu\mu\gamma} > 110$ GeV/c^2.

V. CROSS SECTION RESULTS

A. Calculation of the Total $\mu\mu\gamma$ Cross Section

The total cross section for $\mu\mu\gamma$ production is obtained from the ratio of the acceptance-corrected $\mu\mu\gamma$ rate for $M_{\mu\mu} > 60$ GeV/c^2, $\Delta\mathcal{R}(\gamma-\mu) > 0.7$, $p_T^\gamma > 10$ GeV/c^2, and $|\eta^\gamma| < 1$, to the total acceptance-corrected dimuon rate for $M_{\mu\mu} > 60$ GeV/c^2, where $\Delta\mathcal{R}(\gamma-\mu)$ is again defined for the photon and the nearest muon, and η^γ is the psuedorapidity defined with respect to the interaction point and the beam direction. This ratio is multiplied by the total cross section for $\mu\mu$ production for $M_{\mu\mu} > 60$ GeV/c^2, calculated with the FEWZ next-to-next-to-leading-order (NNLO) generator [6] with the CTEQ66 PDF. The FEWZ central value is 262.9 ± 8.0 pb, where the dominant uncertainty is from the choice of PDF. We use this method because uncertainties in the muon trigger efficiencies, reconstruction efficiencies, and luminosity are large. The expression for the $\mu\mu\gamma$ cross section is:

$$\sigma_{Z\gamma} \times \mathcal{B} = \frac{\kappa N^{data}_{\mu\mu\gamma} \left(A_{cc} \times \epsilon_{ID}\right)^{-1}_{\mu\mu\gamma}}{N^{data}_{\mu\mu} \left(A_{cc} \times \epsilon_{ID}\right)^{-1}_{\mu\mu}} \times (\sigma_Z \times \mathcal{B})^{NNLO}_{FEWZ}, \tag{2}$$

where the parameter $\kappa \approx 0.85$ is estimated with PYTHIA and corrects for the fraction of events that do not pass generator-level requirements but are contained in the acceptance of the data sample because of the detector resolution. Here, $\sigma_{Z\gamma}$ and σ_Z are the total cross sections for $Z\gamma$ and Z production, respectively. The term $\mathcal{B}$ is the branching fraction for $Z \to \mu\mu$, which is the standard model is ≈ 0.033.

We use a full simulation of the detector to estimate the acceptance and efficiencies as a function of p_T^γ. For the events that pass generator-level requirements, the product of acceptance and identification efficiency, $A_{cc} \times \epsilon_{ID}$, provides the fraction of events that pass the analysis requirements with all acceptance measured relative to the aforementioned kinematic requirements at the generator-level. Events migrate between bins in p_T^γ because of detector resolution, and these effects are taken into account in calculating $A_{cc} \times \epsilon_{ID}$ as a function of p_T^γ.

B. Systematic Uncertainties

To account for events in the reconstructed sample which do not pass generator-level cuts, the candidate sample is corrected for by including a parameter κ in the definition of the cross section, as given in Eq. (2). We vary the number of events produced outside the generator-level cuts in the PYTHIA simulation by $\pm 20\%$ to estimate the systematic uncertainty in the final cross section measurement. We find that the effect introduced a 1.5% systematic uncertainty on the total cross section.

The dominant uncertainty corresponding to the calculation of $A_{cc} \times \epsilon_{ID}$ is due to choice of PDF. There are 20 free parameters in the CTEQ6.1L parameterization of the PDF. These parameters reflect fits to collider data, and the uncertainties on acceptance and efficiencies are estimated by gauging the effect of varying the 20 parameters of the CTEQ6.1M PDF relative to their central values [8]. We find a total PDF uncertainty of 3.3%, dominated by the uncertainty in extrapolating the acceptance of muon kinematics to the full phase space.

The photon ID efficiency is estimated from a simulated sample of photons in a simulation of the full detector, and is estimated to have an uncertainty of 10% for $p_T^\gamma < 15$ GeV/c and 3% for $p_T^\gamma > 15$ GeV/c.

C. Total $\mu\mu\gamma$ Cross Section Results

The total cross section extracted for $Z\gamma$ production in the muon channel using the matrix method with $M_{\mu\mu} > 60$ GeV/c^2, $p_T^\gamma > 10$ GeV/c, $|\eta^\gamma| < 1$, and $\Delta\mathcal{R}(\gamma - \mu) > 0.7$ is $\sigma_{Z\gamma} \times \mathcal{B} = 1.16 \pm 0.05$ (stat.) $\pm$ 0.10 (syst.) pb, which includes both FSR and ISR contributions. The result is consistent with the MCFM NLO prediction of $\sigma_{Z\gamma} \times \mathcal{B} = 1.10$ $\pm$ 0.03 (syst.) pb with CTEQ66 PDF and the renormalization and factorization scales evaluated at the mass of the W boson, $M_W = 80$ GeV/c^2 [7].

To reduce the size of the FSR contribution, we also quote results for the additional requirement that the three-body invariant mass $M_{\mu\mu\gamma} >$110 GeV/c^2. For this, we measure $\sigma_{Z\gamma} \times \mathcal{B} = 0.31 \pm 0.03$ (stat.) $\pm$ 0.02 (syst.) pb, which is consistent with the MCFM NLO prediction of $\sigma_{Z\gamma} \times \mathcal{B} = 0.29 \pm 0.01$ (syst.) pb.

D. Differential Cross Section $d\sigma/dp_T^\gamma$

We use matrix-inversion to unfold the experimental resolution to extract the differential cross section as a function of p_T^γ. For notational simplicity, the term $d\sigma/dp_T^\gamma$ signifies the differential cross section for $Z\gamma \to \mu\mu\gamma$ production. The elements of the smearing matrix between p_T^γ bins are estimated from a PYTHIA simulation and are used to the invert the matrix to obtain the unsmeared spectrum, as oulined in Ref. [9]. The unfolded differential cross sections for data are compared to the NLO MCFM predictions with and without a $M_{\mu\mu\gamma} > 110$ GeV/c^2 requirement, as shown in Fig. 5 and Fig. 6. Following Ref. [10], the position of the data points are corrected by plotting the value of p_T^γ where the cross section equals the average value for that bin. We recalcluate the NLO MCFM calculation with the renormalization and factorization scales set to 160 GeV/c^2 and again at 40 GeV/c^2 and use these as ± 1 standard deviations on the theoretical uncertainty of the unfolded data relative to the central NLO MCFM value (which assumes a scale of 80 GeV/c^2). The values of the unfolded differential cross section for each p_T^γ bin are given in Table I and Table II.

VI. CONCLUSIONS

We have measured the corrected differential and total cross sections for $\mu\mu\gamma$ production for no $M_{\mu\mu\gamma}$ requirement and for $M_{\mu\mu\gamma} > 110$ GeV/c^2 in $p\bar{p}$ collisions with a center of mass energy $\sqrt{s} = 1.96$ TeV at the Fermilab Tevatron Collider. Both the total cross section and the differential cross section as a function of p_T^γ are consistent with the SM at NLO predicted by the MCFM generator.

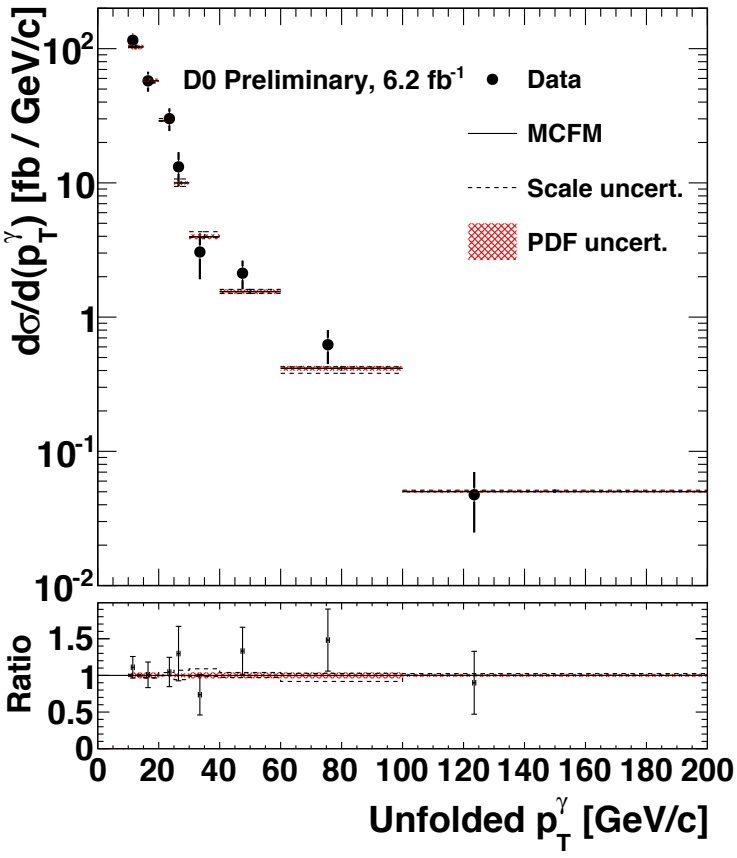

FIG. 5: The corrected differential cross section in p_T^γ, with data points placed at p_T^γ that correspond to the mean $d\sigma/dp_T^\gamma$ in that bin, compared to the standard model NLO MCFM prediction with no $M_{\mu\mu\gamma}$ requirement. The ratio shown at the bottom is between data and the NLO MCFM prediction, and is compared to fractional theoretical uncertainties on the central NLO MCFM values arising from the choice of PDF and QCD scale.

		Data - Bkgd [fb/GeV/c]	NLO MCFM [fb/GeV/c]
p_T^γ bin [GeV/c]	p_T^γ center [GeV/c]	$d\sigma/dp_T^\gamma$	$d\sigma/dp_T^\gamma$
10 - 15	12.4	115.54 ± 7.11 ± 13.74	104.02 ± 4.10
15 - 20	17.2	57.68 ± 7.25 ± 6.44	57.13 ± 2.23
20 - 25	22.5	30.11 ± 5.44 ± 1.81	28.77 ± 0.43
25 - 30	27.5	13.28 ± 3.64 ± 0.89	10.16 ± 0.26
30 - 40	34.4	3.06 ± 1.12 ± 0.20	4.15 ± 0.16
40 - 60	48.5	2.12 ± 0.50 ± 0.11	1.60 ± 0.061
60 - 100	76.5	0.62 ± 0.17 ± 0.04	0.42 ± 0.017
100 - 200	124.5	0.047 ± 0.023 ± 0.002	0.052 ± 0.001

TABLE I: The unfolded differential cross section $d\sigma/dp_T^\gamma$ for data and for NLO MCFM with data corrected on the mean value of $d\sigma/dp_T^\gamma$ with no $M_{\mu\mu\gamma}$ requirement. Uncertainties on PDF are included for the NLO MCFM prediction.

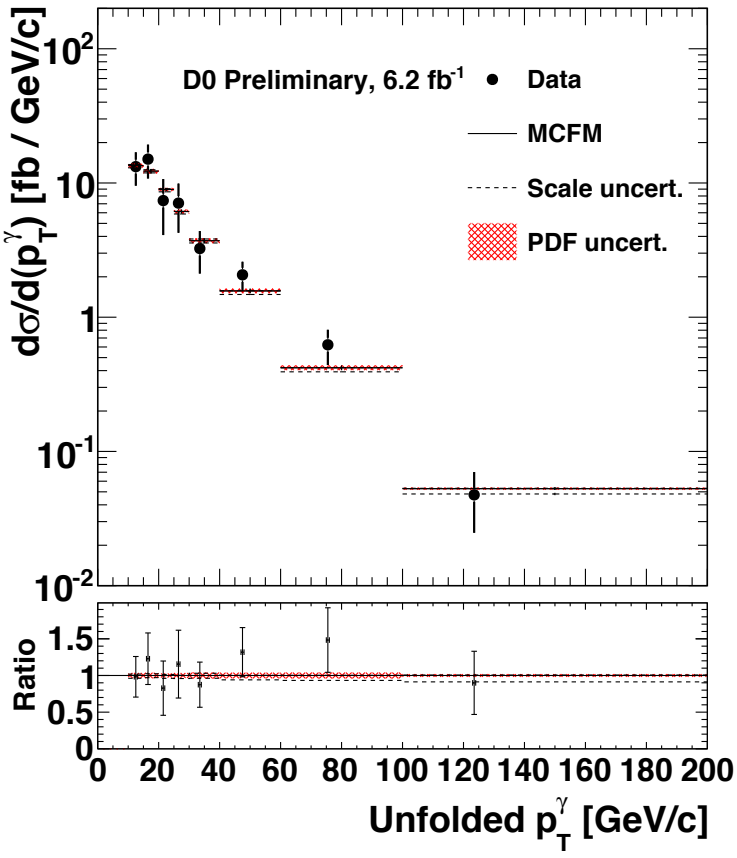

FIG. 6: The corrected differential cross section in p_T^γ for $M_{\mu\mu\gamma} > 110$ GeV/c^2, with data points placed at p_T^γ that correspond to the mean $d\sigma/dp_T^\gamma$ in that bin, compared to the standard model NLO MCFM prediction. The ratio shown at the bottom is between data and the NLO MCFM prediction, and is compared to fractional theoretical uncertainties on the central NLO MCFM values arising from the choice of PDF and QCD scale.

		Data - Bkgd [fb/GeV/c]	NLO MCFM [fb/GeV/c]
p_T^γ bin [GeV/c]	p_T^γ center [GeV/c]	$d\sigma/dp_T^\gamma$	$d\sigma/dp_T^\gamma$
10 - 15	13.7	13.24 ± 3.31 ± 1.76	13.48 ± 0.48
15 - 20	17.2	15.06 ± 3.86 ± 1.82	12.25 ± 0.47
20 - 25	22.0	7.40 ± 3.18 ± 0.88	8.94 ± 0.25
25 - 30	27.4	7.08 ± 2.73 ± 0.70	6.13 ± 0.21
30 - 40	34.5	3.24 ± 1.087 ± 0.33	3.71 ± 0.15
40 - 60	48.6	2.07 ± 0.49 ± 0.16	1.57 ± 0.061
60 - 100	76.5	0.62 ± 0.17 ± 0.059	0.42 ± 0.017
100 - 200	124.5	0.047 ± 0.023 ± 0.002	0.053 ± 0.001

TABLE II: Summary of the unfolded differential cross section $d\sigma/dp_T^\gamma$ for the data and for NLO MCFM with bin-centering corrections and $M_{\mu\mu\gamma} > 110$ GeV/c^2. PDF uncertainties are included for the NLO MCFM prediction.

Acknowledgments

We thank the staffs at Fermilab and collaborating institutions, and acknowledge support from the DOE and NSF (USA); CEA and CNRS/IN2P3 (France); FASI, Rosatom and RFBR (Russia); CNPq, FAPERJ, FAPESP and FUNDUNESP (Brazil); DAE and DST (India); Colciencias (Colombia); CONACyT (Mexico); KRF and KOSEF (Korea); CONICET and UBACyT (Argentina); FOM (The Netherlands); STFC and the Royal Society (United Kingdom); MSMT and GACR (Czech Republic); CRC Program and NSERC (Canada); BMBF and DFG (Germany); SFI (Ireland); The Swedish Research Council (Sweden); and CAS and CNSF (China).

[1] V.M. Abazov, *et al.*, Nucl. Instrum. Methods in Phys. Res. A **565**, 463 (2006);
V.M. Abazov, *et al.*, Nucl. Instrum. Methods in Phys. Res. A **552**, 372 (2005);
S.N. Ahmed, *et al.*, Nucl. Instrum. Methods in Phys. Res. A **634**, 8 (2011);
R. Angstadt, *et al.*, Nucl. Instrum. Methods in Phys. Res. A **622**, 298 (2010).
[2] V.M. Abazov, *et. al.*, Phys. Rev. Lett. **102**, 231801 (2009).
[3] E. Barberio, *et. al.*, Comput. Phys. Commun. **79**, **291** (1994). PHOTOS v2.0 is used.
[4] V.M. Abazov, *et. al.*, Phys. Rev. Lett. **100**, 102002 (2008).
[5] R. Brun, F. Carminati, CERN Program Library Long. Writeup W5013, 1993 (unpublished).
[6] R. Gavin, Y. Li, F. Petriello, S. Quackenbush, [arXiv:1011.3540 [hep-ph]];
K. Melnikov, F. Petriello, Phys. Rev. D **74**, 114017 (2006).
[7] J. Campbell, R. Ellis, C. Williams, JHEP **1107**, 018 (2011).
[8] D. Stump, *et. al.* JHEP **0310**, 046 (2003)
[9] G. Cowan, *Statistical Data Analysis* (Oxford University Press, USA, 1998), Chapter 11.
[10] G.D. Lafferty, T.R. Wyatt, Nucl. Instrum. Methods in Phys. Res. A **355**, 541 (1995).